INTERNATIONAL JOURNAL OF AUTOMOTIVE AND MECHANICAL ENGINEERING
ISSN: 2229-8649 e-ISSN: 2180-1606
VOLUME 22, ISSUE 3, 2025, 12801 - 12820
DOI: https://doi.org/10.15282/ijame.22.3.2025.19.0976

RESEARCH ARTICLE

Transient Analysis of Railway Curve Squeal Using the Finite Element Method

Charvinder Singh[1]*, Zaidi Mohd Ripin[1], Nurul Farhana Mohd Yusof[1], Muhammad Fauzinizam Razali[1], Muhammad Najib Abdul Hamid[2]

[1]The Vibration Lab, School of Mechanical Engineering, Engineering Campus, Universiti Sains Malaysia, 14300 Nibong Tebal, Pulau Pinang, Malaysia
[2]Malaysian Spanish Institute, Universiti Kuala Lumpur,09000 Kulim, Kedah, Malaysia

ABSTRACT – Railway curve squealing refers to the repeated emission of a high-pitched sound caused by the interaction between train wheels and curved rail sections. This high-frequency noise creates significant discomfort for both passengers and nearby residents. The phenomenon arises from frictional interaction between the wheel and rail, governed by a yaw angle that generates lateral forces. These forces result from increased sliding velocity in the contact area due to the angular motion of the wheel, leading to dynamic instability. To investigate this, a finite element model of a twin-disk system was developed, and a time-domain nonlinear transient analysis was performed. The lateral nodal displacements of the wheel within the contact patch were examined during its interaction with the rail, assuming a constant friction coefficient. The displacement nodes exhibited an oscillatory response characteristic of stick–slip motion, which continuously excites the wheel–rail system. These oscillations indicate that the wheel is the primary source of squeal and match the measured squeal frequency of 2400 Hz, thereby validating the twin-disk model. During curving, lateral creepage occurs at the contact interface, inducing self-excited vibrations that manifest as squeal.

ARTICLE HISTORY

Received	:	27th Nov. 2024
Revised	:	28th May 2025
Accepted	:	01st Aug. 2025
Published	:	05th Oct. 2025

KEYWORDS
Railway curve squeal
Stick–slip phenomenon
Finite element method
Twin-disk system
Friction coefficient
Nodal lateral displacement

1. INTRODUCTION

Squeal noise is referred to as a high magnitude disturbance typically observed when a train operates on a tight-curve track. This phenomenon, known as railway curve squealing, generates vibrations and disturbances that pose persistent challenges for railway systems, affecting the environment, passengers, and nearby residents [1]. Squealing noise occurring at the curve is a complex, multifaceted issue that has persisted over the years and has become the subject of extensive research [2]. Its frequencies generally range from 250 to 5000 Hz, with reported sound pressure levels between 110 and 130 dBA [3,4], about 20 dBA higher than rolling noise [5]. This high-frequency tonal noise occurs when the wheel–rail interface undergoes self-excited vibration.

Tangential forces—comprising vertical, lateral, and longitudinal components—are generated when a train traverses a curved track. Lateral forces during curving can cause plastic deformation, potentially leading to wheel damage known as tread rollover [6]. As observed in [7], high lateral forces acting on the wheel result in elevated lateral rail vibration, which manifests as squealing. Lateral creepage at the contact interface is the principal factor driving this instability. It arises from self-excitation induced by decreasing friction, which introduces negative equivalent damping into the system, producing squeal [8, 9]. According to [10], lateral creepage increases as the radius of curvature diminishes, making the system prone to self-excited frictional vibrations and thus squeal.

Rudd [11] attributed the phenomenon to stick–slip motion, whereby increased sliding velocity reduces friction, transferring energy into the system and destabilizing it. The nonlinear behavior of creep forces can form a limit cycle, allowing unstable oscillations to grow. Rudd's findings regarding diminishing friction have been broadly acknowledged and further refined by subsequent studies. Wickens [12] observed that, while curving, sliding velocity arises at the contact patch as the wheel gains a significant angle of attack relative to the direction of motion. Kalker [13] defined this sliding velocity, normalized by running velocity, as “creepage,” consisting of two translational and one rotational component, each contributing to creep force generation. The coefficient of adhesion, which associates perpendicular contact force with directional force, reduces with elevated creepage, resulting in a negative slope in the friction–creepage curve [9,14].

The primary parameter influencing lateral creepage is the curve radius [8,15]. Sharper curves increase the yaw angle, resulting in increased lateral creepage and, consequently, greater lateral loads. Thompson et al. [16] used numerical modeling to confirm that lateral creepage is central to squeal onset by inducing unstable vibrations, and found it to be equivalent to the angle of attack. Similar results in [17] showed that tighter curves increase lateral creep force, producing a negative slope in the friction curve [18]. Xie et al. [19], building on De Beer et al. [20], incorporated falling-friction effects at various curve radii into a steady-state curving analysis. They found squeal to be most pronounced between 150 m and 250 m radii, with falling creep stresses observed on the front wheels, while the rear wheels did not squeal because they did not reach the lateral creep force threshold.

***CORRESPONDING AUTHOR | C. Singh** | ✉ charvinder@student.usm.my

Liu and Meehan [21] investigated squeal in relation to lateral adherence using a dual-disk rig to simulate wheel misalignment and rail contact. They concluded that lateral creepage, rather than flange contact or longitudinal slip, was the primary source of energy for squeal. Reducing the friction levels at the interface of the contacting surfaces has been shown to lower the propensity for squeal [22]. Effective mitigation measures include friction modifiers, such as water- and oil-based top-of-rail formulations. Water-based modifiers can reduce sound pressure by up to 17 dB in twin-disk tests [23], though their effectiveness diminishes at higher angles of attack [24]. Oil-based modifiers [25] can also reduce squeal but may not eliminate it, and can pose braking safety risks by lowering adhesion [26]. As observed in [27], the use of grease at the contact interface has been shown to reduce the propensity for squeal; however, it must be applied carefully to avoid adhesion loss.

Ring-damped wheels offer another mitigation strategy. As reported in [28], they can increase modal damping by 334%–614% compared to regular wheels, substantially reducing squeal levels. However, these tests did not incorporate pre-load or realistic wheel–rail contact conditions. Time-domain analyses [29–31] indicate that shifting the contact point toward the field side increases stick–slip oscillations; thus, optimizing wheel designs to shift the contact patch may reduce squeal, although this approach has not yet been implemented [32]. A more recent method involves applying dither signals to disrupt the build-up of self-excited vibrations [32], though practical application would require fast and cost-effective retrofitting.

The first time-domain representation for curve squeal was established by Scheinder and Popps [33], incorporating Milind's theory to identify wheel eigenvalues and mode shapes. They found that wheels with low rim mass and high web stiffness tend to produce higher squeal levels. Heckl and Abrahams [34] modeled the wheel as a flat circular surface with contact forces derived from Green's function, later extending the model into the frequency domain to assess mode stability [35]. Glocker et al. [36] applied Coulomb's constant-friction model, concluding that squeal occurs when normal and tangential motions are coupled in the contact zone. Pieringer [37] combined normal and tangential dynamics in a nonlinear rolling contact model based on Kalker's theory, also using Coulomb friction. These studies collectively highlight the roles of lateral creepage, contact position, and friction in curve squealing.

Most existing work examines squeal by analyzing lateral forces and sliding across the entire contact patch. However, the role of individual nodal contacts within the patch has not been explored. This study addressed that gap by focusing on the oscillatory behavior of a specific wheel node as it enters and exits the rail contact region. A finite element (FE) representation of a twin-disk system was created to conduct a time-domain transient dynamic analysis of lateral nodal displacements. The analysis simulates rolling at 0.5 rad/s with a yaw angle of –3° to replicate curvature effects. The FE model is validated through experimental modal analysis, and the nodal oscillatory response is compared with squeal measurements obtained from the twin-disk rig.

2. METHODOLOGY

This section outlines the research methodology, including the creation, description, and transient analysis of the FE model used in this study.

2.1 Stick-Slip Mechanism

Figure 1 illustrates the twin-disk system, wherein the upper disk represents the wheel and the lower disk the rail. Applying a non-zero yaw misalignment between the wheel-rail interface induces a lateral relative velocity, normalized by the rolling velocity—known as lateral creepage. This creepage generates substantial creep forces, which, in sharp curves, reach a saturation point (creep saturation). Beyond this threshold, further increases in creepage cause the coefficient of friction to decrease, a phenomenon referred to as negative friction. This negative friction leads to stick-slip oscillations at the contact region, resulting in wheel resonance and consequent noise emission, as noted by Thompson et al. [38] and Eadie et al. [39]. This study simulated a curve with a yaw angle of -3°, allowing both the wheel and rail to roll along the Z-axis, which is the direction of travel. Lateral creepage occurs when the wheel forms a yaw angle relative to the rail.

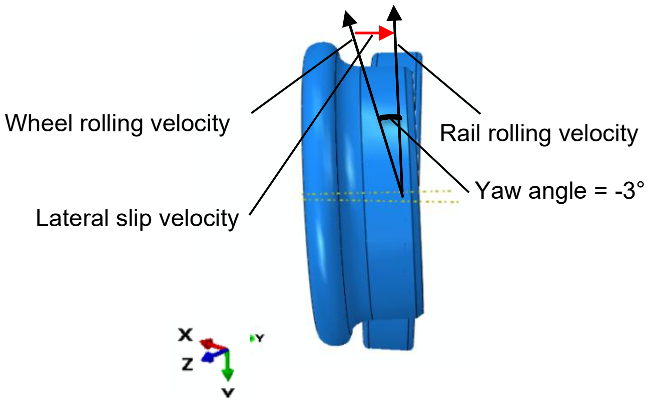

Figure 1. Schematic of the twin-disk system, illustrating the wheel and rail system

$$V_{slide} = V_{wheel} - V_{rail}. \tag{1}$$

During curve negotiation, a relative sliding velocity arises at the wheel-rail interface due to the differences in motion in the wheel's rolling direction and the rail. It is expressed as in Equation 1, where V_{wheel} denotes the velocity of the wheel at the contact location, and V_{rail} represents the velocity of the rail at the contact point. The equation can be expressed as a function of time.

$$m\ddot{U}(t) + c\dot{U}(t) + kU(t) = F(\mathrm{t}) \tag{2}$$

where $\ddot{U}(t), \dot{U}(t)$ and $U(t)$ denote the lateral acceleration, velocity, and displacement at the contact patch, respectively. The frictional force acting at the contact patch is denoted by F, while *m*, *c*, and *k* correspond to the system's mass, damping coefficient, and stiffness, respectively. The stick–slip phenomenon consists of two distinct phases. In the sticking phase, the condition is defined by $F < \mu_s N$, where μ_s is the static friction coefficient. In this phase, the wheel and rail move at the same velocity. In the sliding phase, motion begins when the lateral force exceeds the friction threshold, expressed as $F = \mu_d N$, where µd is the dynamic friction coefficient. As the dynamic coefficient decreases and the relative sliding velocity increases, a constant energy feedback mechanism is triggered. The dynamic coefficient varies inversely with the sliding velocity, making it a key factor in driving instability. The force term in the motion equations characterizing the system is attributed to frictional interaction at the nodes as the disks rotate and undergo lateral displacement. The constant friction coefficient used in the analysis indicates that curve squeal primarily results from persistent stick–slip motion, which continuously excites both disks during rotation. This interaction produces an oscillatory limit cycle, generating the high-amplitude vibrations characteristic of curve squeal.

2.2 Transient Dynamic Analysis

A convergence evaluation for the mesh was conducted before the transient analysis. The wheel–rail system was meshed using linear hexahedral (C3D8I) elements. Employing a finer mesh in finite element analysis is essential, as it produces more accurate results without unnecessarily increasing computational cost. As noted in [40], obtaining accurate and reliable results depends heavily on selecting an optimal mesh model without increasing computational load. Coarse meshes containing fewer than 5000 elements may produce unreliable outcomes, whereas hexahedral elements generally yield higher accuracy than tetrahedral elements [40]. Eight convergence simulations were conducted to investigate the correlation between contact pressure and element dimensions within the contact zone. (Figure 2). Beyond point P8, further mesh refinement had minimal impact on contact pressure. At point H, the contact area had an element size of 0.6 mm and a maximum contact pressure of 819 MPa; thus, 0.6 mm was adopted as the optimal mesh size.

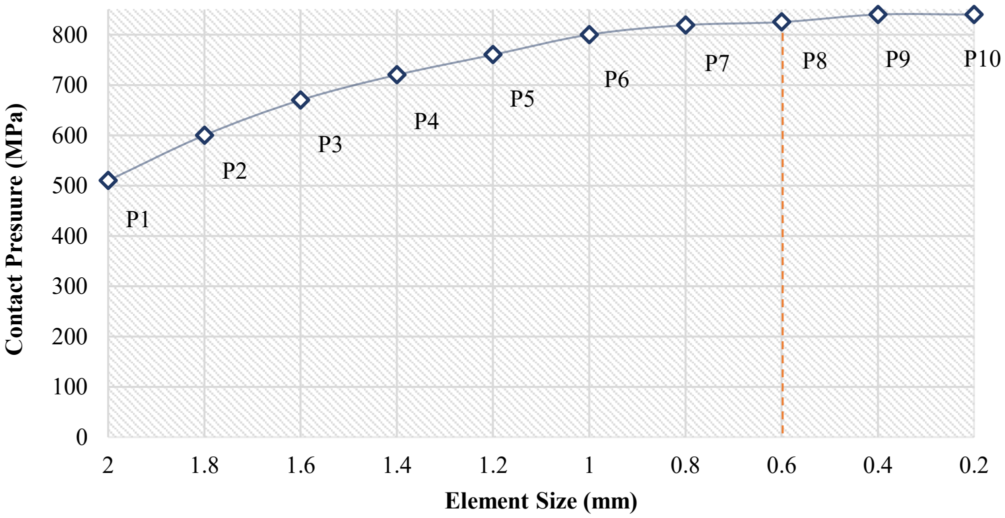

Figure 2. Mesh convergence

This study employed the FE method to analyze the system's dynamic behavior during the transient phase. The wheel-rail system is represented by a twin-disk FE system utilizing Abaqus 6.13. The wheel is modelled using a combination of linear hexahedral (C3D8R) elements. The element at the contact region was refined to a mesh size of 0.6 mm to ensure accuracy, as illustrated in Figure 3. The model included 900,615 hexahedral elements. The rail was composed entirely of linear hexahedral elements (C3D8R). In this analysis, the Z-axis represents the travel direction, the X-axis signifies angular motion, and the Y-axis indicates translational displacement in the vertical direction.

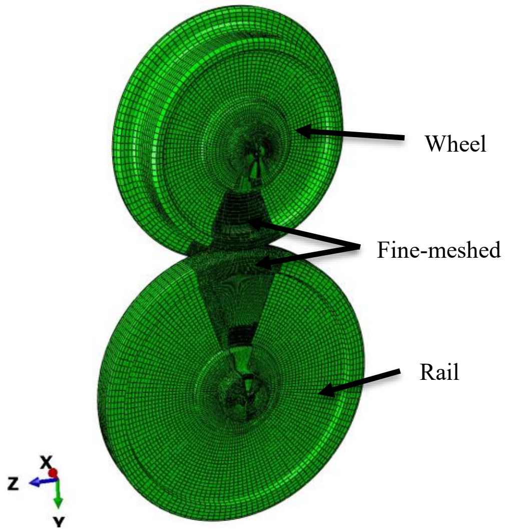

Figure 3. FE model

Both the wheel and rail were modeled in steel. The rail geometry was based on the UIC 60 standard, and the wheel geometry followed the S1002 standard. The corresponding dimensions are shown in Figures 4 and 5. The model's mechanical parameters are listed in Table 1. Both components were represented as solid, deformable, fully elastic structures.

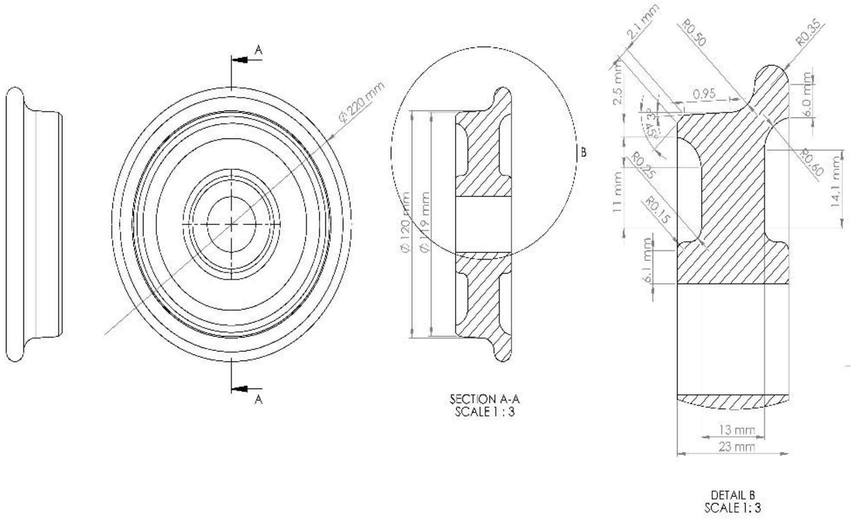

Figure 4. Wheel dimensions in mm

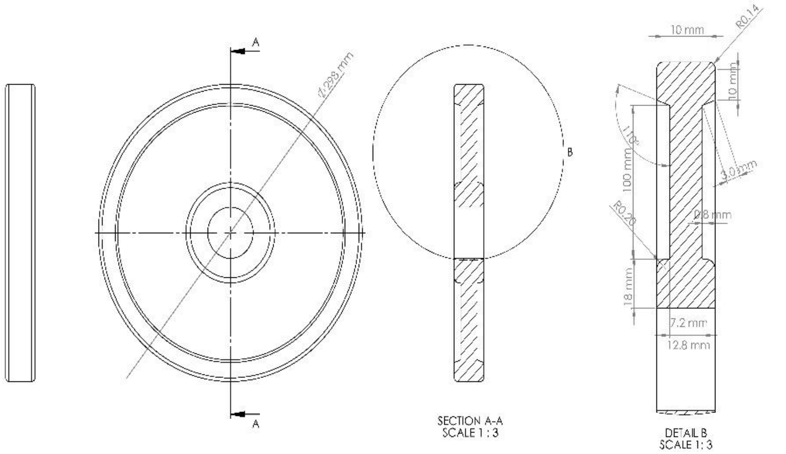

Figure 5. Rail dimensions in mm

Table 1. Mechanical properties of both the rail and wheel

Mechanical Properties	
Young's Modulus, E	210 GPa
Yield Strength	545 MPa
Poisson's Ratio	0.3
Density	7590 kg/m^3

To examine the nonlinear transient response in the contact area, the following three procedures were used:

Step 1: A nonlinear static step was employed to establish wheel–rail contact. The wheel was rotated about the Y-axis to achieve a yaw angle of –3°, as shown in Figure 1 (Section 2.1), representing the relative yaw angle during curve negotiation. The contact was defined using a surface-to-surface contact with tangential and normal characteristics. The wheel was identified as the principal surface, while the rail was classified as the secondary surface. A finite sliding formulation with a penalty method was employed, utilizing a coefficient of friction of $\mu = 0.35$, characterized by tangential behavior and hard contact for normal behavior.

Step 2: Pre-loading phase: During this stage, a dynamic explicit step was implemented, and rolling motion was generated by integrating boundary conditions into both the wheel and rail. Abaqus employs a global coordinate system characterized by translational displacements U1, U2, and U3, corresponding to the X, Y, and Z axes, respectively. The angular motion is denoted as UR1, UR2, and UR3, representing the rotating motion about the X, Y, and Z axes, respectively.

The displacement/rotation boundary conditions, denoted as RP1 and RP2, were applied, as shown in Figure 6. The inner shaft surfaces of both the wheel and rail were coupled to a reference point with displacement/rotation boundary conditions applied. The wheel's boundary conditions were constrained in all directions except for the U2 direction, which is associated with translation motion along the Y-axis. A rotational velocity of 0.5 rad/s was applied in the UR1 direction, which associated rotation motion along the X-axis, facilitating both pre-loading effects and rolling motion. For the rail, all boundary conditions were constrained in every direction except the U1, which governs the lateral effect and UR1 direction, which pertains to the rotating motion around the X-axis, where a rotational speed of 0.5 rad/s is imposed to facilitate rolling motion. A concentrated force of 1200 N, simulating the carriage's weight, was applied to the wheel in the vertical direction. Additionally, to mimic the effects of curvature, the rail was subjected to a lateral force of 1200 N.

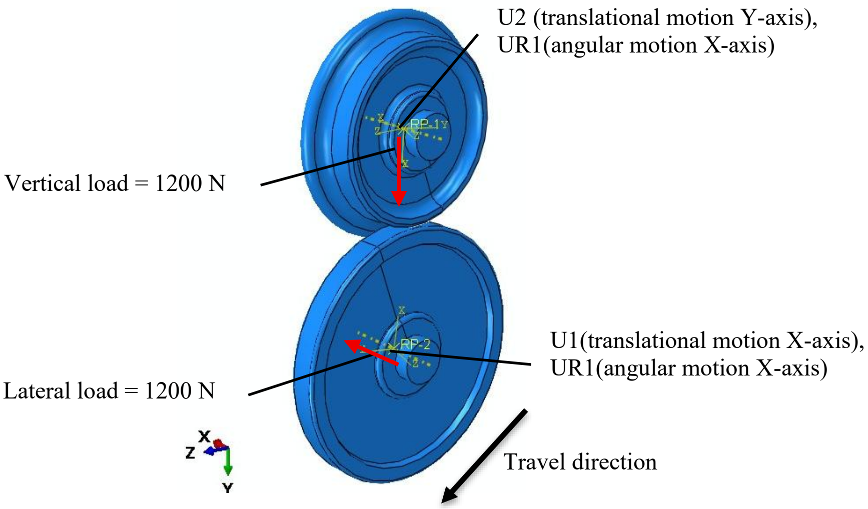

Figure 6. Boundary conditions imposed

Step 3: The nodes, highlighted in green, on the wheel surface are represented in Figure 7, which were utilized to evaluate the lateral response, specifically in the contact region, by tracking the lateral displacement. This stage employs a nonlinear dynamic explicit step to calculate the wheel nodal lateral displacements in the contact region along the U1 (X-axis) direction.

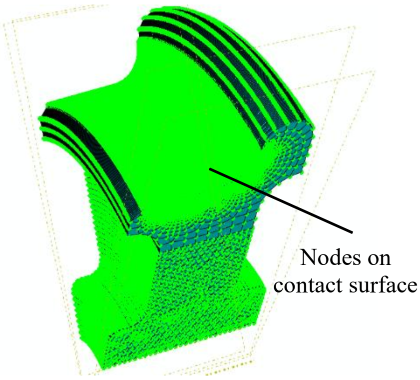

Figure 7. Wheel structure

2.3 Modal Analysis

The wheel-rail system was subjected to a free-free modal analysis, suspended individually using flexible cables, to extract its natural frequencies, damping ratios, and mode shapes. These findings were used to verify the FE model. Measurements were conducted using an LMS Test Lab and a SIEMENS SCADAS mobile acquisition system. A three-axis PCB accelerometer (sensitivity: 10 mV/g) was mounted at Position 2 to record axial acceleration responses. The disk flanges were excited laterally using a B&K 8200 metal-tip impact hammer (sensitivity: 10 mV/N). Sixteen excitation points, evenly spaced at 20.8° intervals around the circumference, were selected (Figure 8). The accelerometer sampling rate was 20,000 Hz, with a frequency bandwidth of 1500–8500 Hz. Each response was averaged over three measurements to ensure reliability.

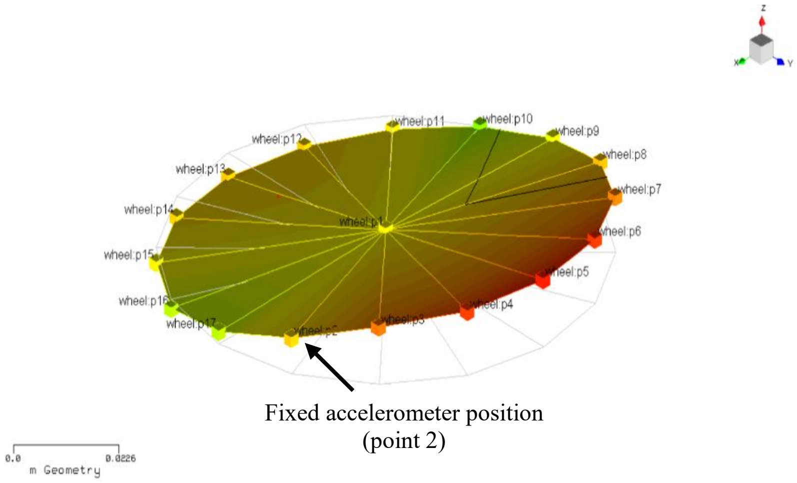

Figure 8. Accelerometer position and excitation points

2.4 Reduced-Scale Rig

A scaled-down twin-disk rig was constructed as shown in Figure 9 to investigate the occurrence of squealing. In a controlled laboratory setting, the wheel–rail interaction is replicated. The rig consisted of an upper and lower disk, which represented the wheel and rail, respectively. Both the disks were free to rotate in the travel direction. However, only the wheel could be rotated about its Y-axis by using the turntable to simulate a yaw angle, thereby inducing a lateral creepage condition. To simulate the roll slip ratio, a 10-kW three-phase induction motor drove the rail independently.

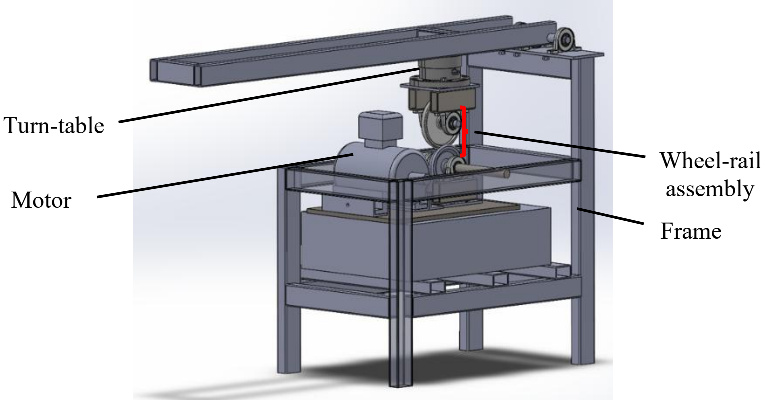

Figure 9. Reduced-scale rig

2.5 Squeal Measurement Test

Squeal measurements were taken in the laboratory with accelerometers mounted at three positions (Figure 10). An integrated-circuit piezoelectric (ICP) microphone, positioned 100 mm from the setup to avoid motor noise, captured the sound. Tests were performed with the wheel rolling at 50 RPM and a yaw angle of −3° to replicate a curve. A National Instruments data-acquisition system enabled real-time monitoring of squeal, vibration modes, and noise levels. LMS TestLab software was used to analyze squeal mode shapes and noise frequency components. The FE model was verified by contrasting these measurements with the findings from the transient dynamic analysis.

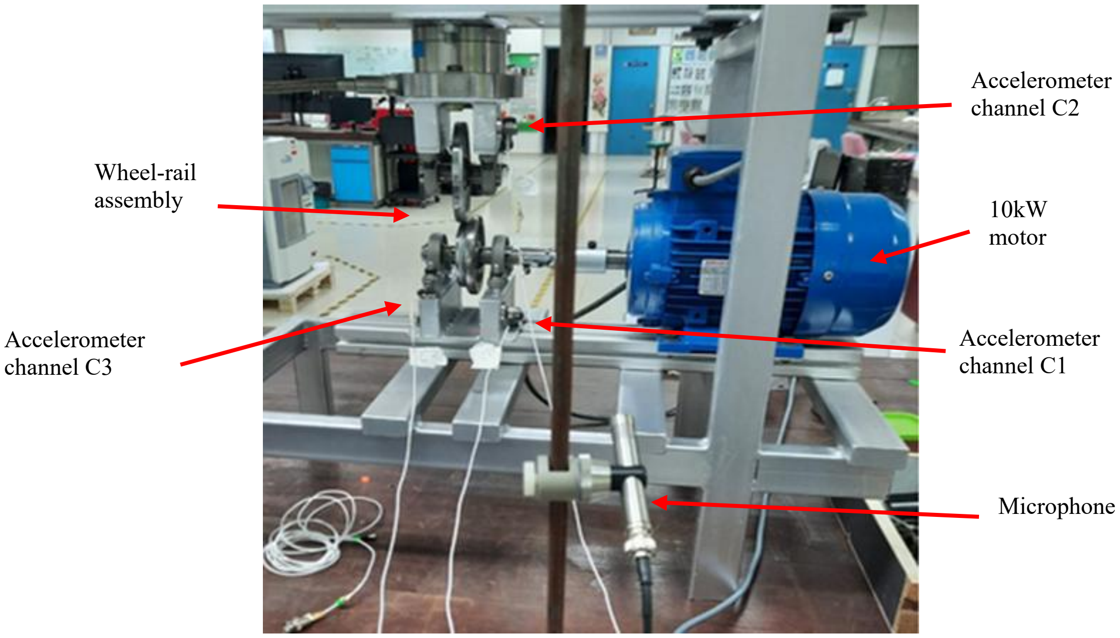

Figure 10. Squeal measurement setup

3. RESULTS AND DISCUSSION

3.1 Model Validation

Using both experimental modal analysis and numerical modal analysis (FE), the natural vibration frequencies and corresponding mode shapes of the system were investigated. The frequency-response-function (FRF) plot, also known as the stabilization diagram (Figure 11), shows the peaks and resonant frequencies obtained from the analysis.

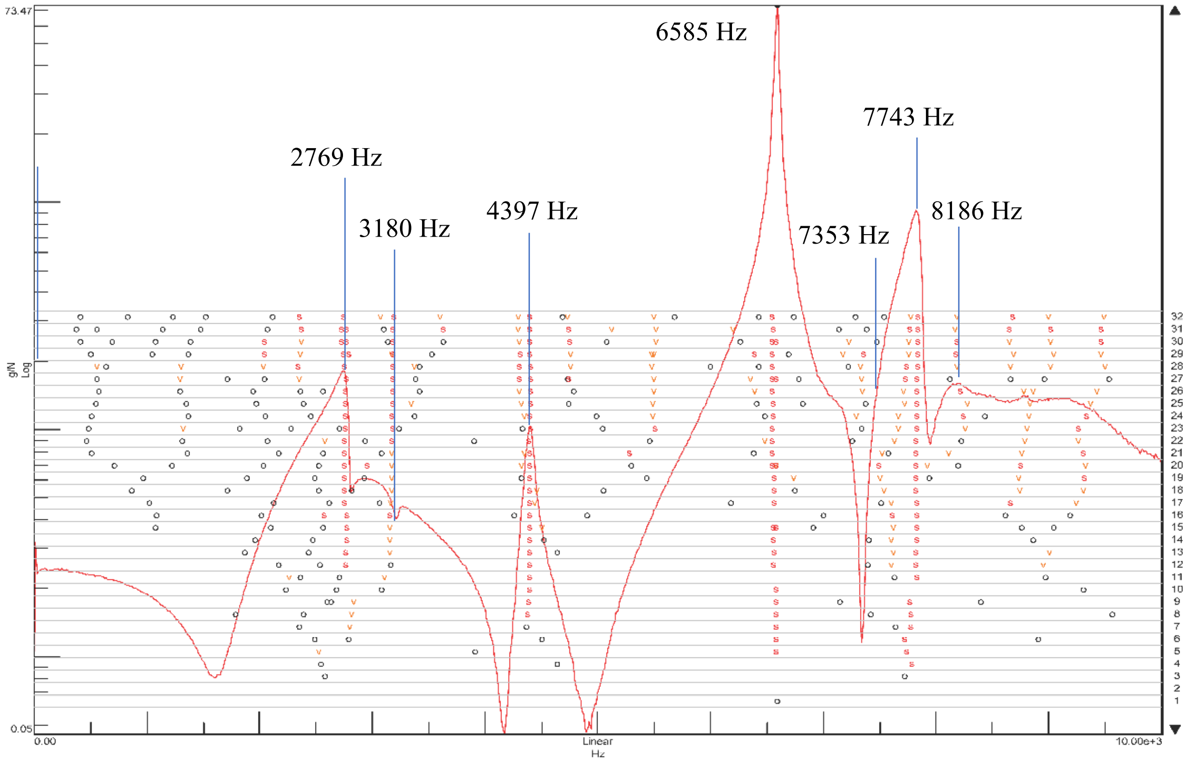

Figure 11. FRF plot of the wheel in the free–free condition

Modal stability was assessed using stabilization diagrams. Stable poles, marked with an "S" symbol, indicate true modes wherein the modal parameters, frequency, damping, and mode shape, are stable and repeatable [41,42]. As described in [43], modes from each iteration were compared to those from the previous iteration to generate the stabilization diagram, a key tool for extracting accurate modal parameters. Seven modes were identified in the frequency range of 2700–8200Hz, with damping ratios ranging from 0.14% to 1.02%, indicating a moderately damped system, as listed in Table 2.

Table 2. Wheel subjected to a free–free condition modal analysis

Mode number	Frequency (Hz)	Damping ratio (%)
1	2769	0.14
2	3180	0.14
3	4397	0.64
4	6585	1.02
5	7353	0.58
6	7743	0.76
7	8186	0.42

Additionally, we conducted a modal analysis on the rail under free conditions, extracting the natural frequencies and mode shapes. The experimental analysis yielded eight modes, as presented in Table 3.

Table 3. Rail subjected to a free–free condition modal analysis

Mode number	Frequency (Hz)	Damping ratio (%)
1	3209	1.25
2	4207	0.83
3	4479	4.33
4	6324	3.02

The calculated natural frequencies ranged from 3209 Hz to 6324 Hz, while the damping ratio varied from 0.14% to 4.33%, indicating a damped structure. The wheel has smaller structural dimensions and lower mass compared to the rail. The frequency-response function (FRF) depicted in Figure 12 compares the peaks from the wheel and rail. The graph indicates that self-excited vibrations may arise at these frequencies and may amplify due to frictional instability caused by lateral creepage. The system's natural frequencies and corresponding mode shapes are subsequently evaluated in the following section against the FE model.

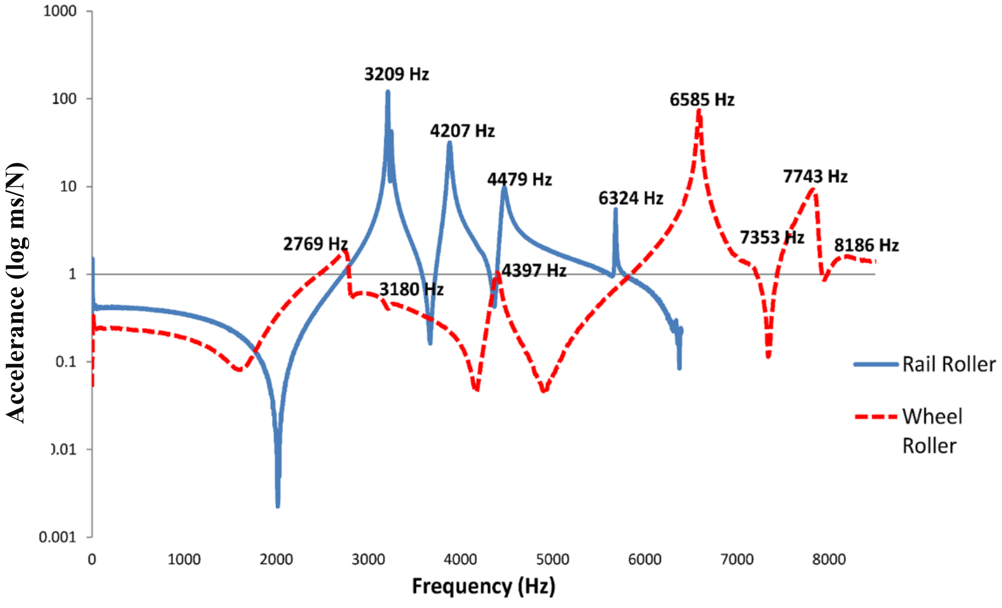

Figure 12. FRF plot of both disks

3.1.1 Experimental versus simulated mode shape validation

Validation plays a crucial role in correlating the results of experimental model analysis with those of the FE model. Therefore, both the rail and wheel are independently validated. In this section, the validation of both the wheel and rail is discussed, followed by the results of the transient dynamic analysis performed. Table 4 presents a comparison of the experimental and simulated natural frequencies. The maximum relative error was below 15.7%. For higher wheel frequencies, the error was consistently below 10%, which falls within an acceptable range. The close correlation across all modes supports the accuracy of the FE model in representing the physical components.

Table 4. Validation of natural frequencies of both disks

	Wheel			Rail		
	Simulation	Experimental	Error %	Simulation	Experimental	Error %
Mode Number	Frequency (Hz)	Frequency (Hz)		Frequency (Hz)	Frequency (Hz)	
1	2393	2769	15.7	3650	3209	12.08
2	3100	3180	2.58	4418	4207	4.77
3	4715	4397	6.74	4800	4479	6.67
4	6205	6585	6.12	7508	6324	15.77
5	7482	7353	1.72			
6	7489	7743	3.39			
7	8759	8186	6.54			

Additionally, to validate the accuracy of the FE modal against the experimental modal analysis, the mode shapes were compared. Tables 5 and 6 illustrate a comparison of the mode shapes of the disks. Because the disks are a key component, the results of experimental and FE analyses should be consistent with each other.

Table 5. Wheel mode shapes

Mode Number	Simulation Mode Shape	Experimental Mode Shape
Mode 1	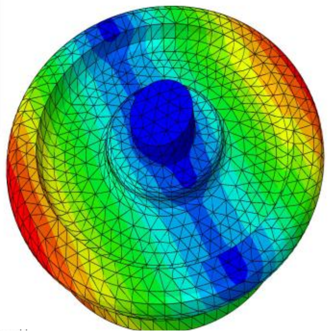 2393 Hz	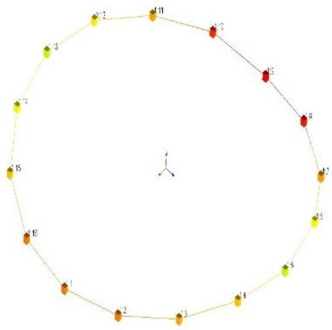 2769 Hz
Mode 2	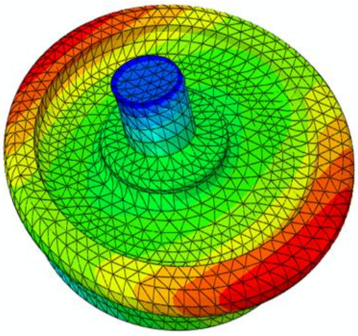 3100 Hz	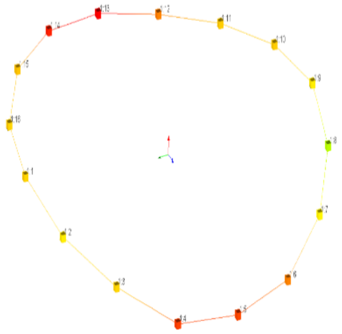 3180 Hz
Mode 3	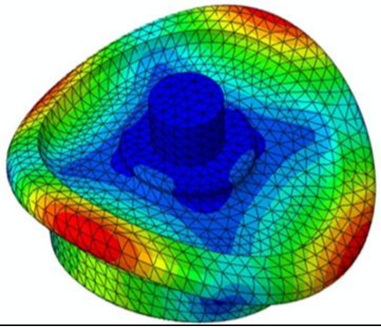	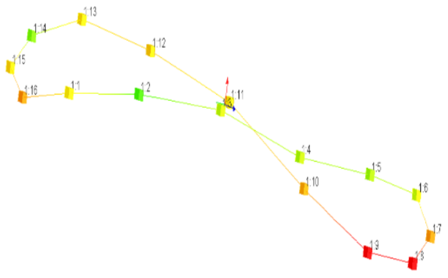

Table 5. (cont.)

Mode Number	Simulation Mode Shape	Experimental Mode Shape
Mode 4	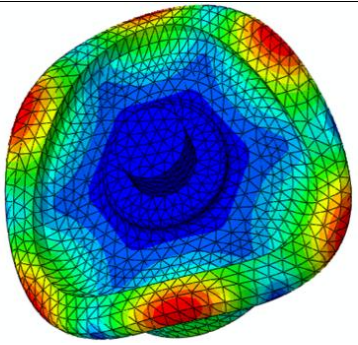 6205 Hz	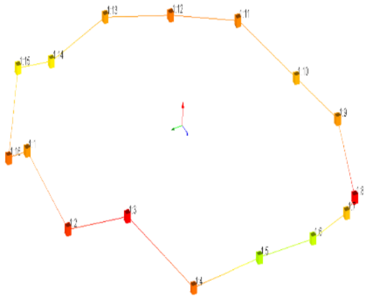 6585 Hz
Mode 5	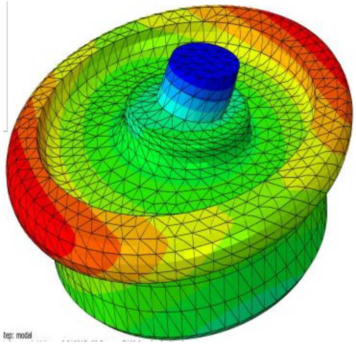 7482 Hz	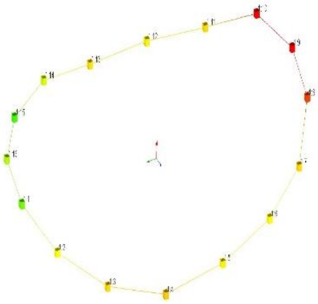 7353 Hz
Mode 6	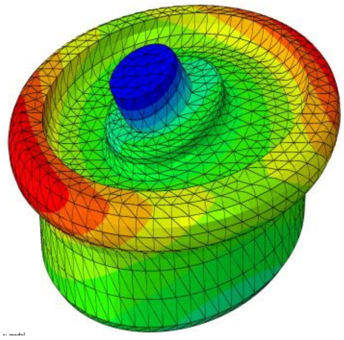 7489 Hz	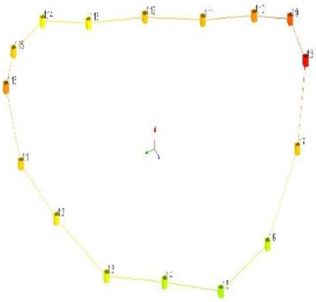 7743 Hz
Mode 7	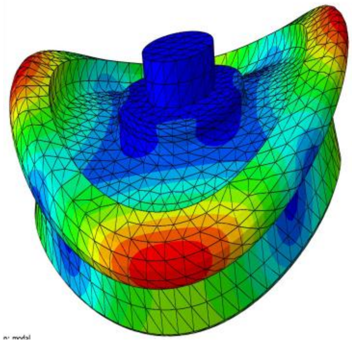 8759 Hz	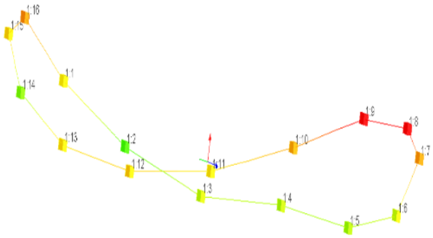 8186 Hz

Table 6. Rail mode shapes

Mode Number	Simulation Mode Shape	Experimental Mode Shape
Mode 1	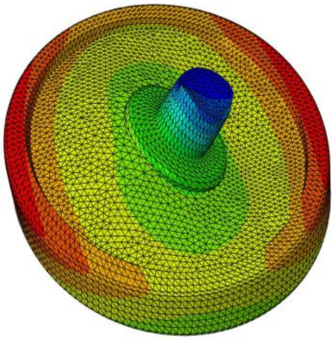 3650 Hz	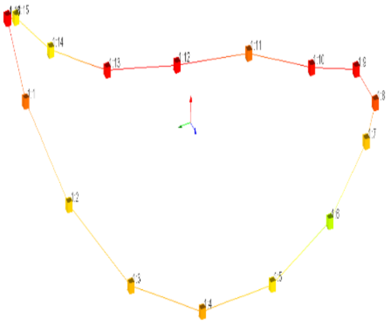 3209 Hz
Mode 2	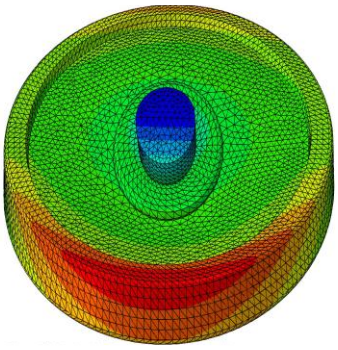 4418 Hz	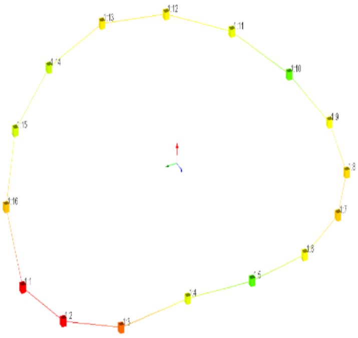 4207 Hz
Mode 3	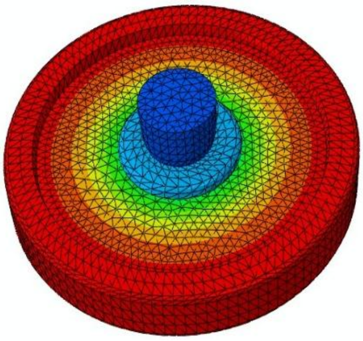 4800 Hz	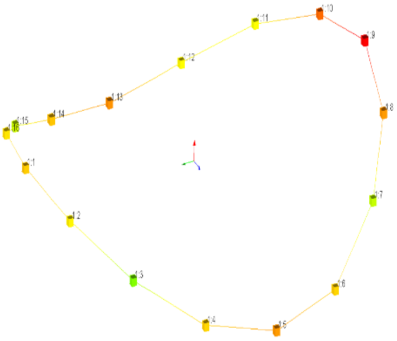 4479 Hz
Mode 4	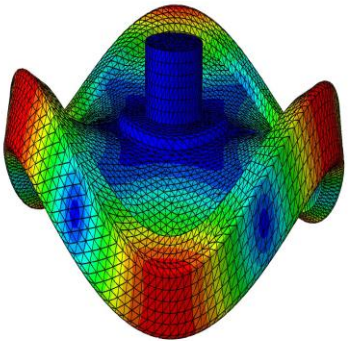 7508 Hz	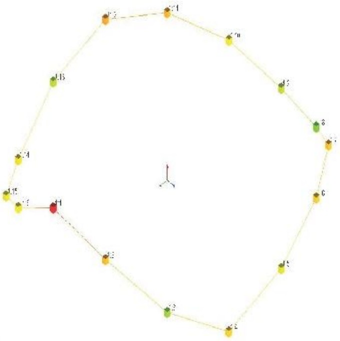 6324 Hz

The FE and experimental modal analysis exhibited a promising correlation, as the variation between the identified natural frequencies of the wheel and those derived from the finite element model is minimal. To further verify the FE model against the experimental modal analysis, a consistency check was performed using the Modal Assurance Criterion (MAC) to assess the mode shapes. As stated in [44], diagonal MAC values approaching 1 indicate a strong correlation with the FE model, whereas values near 0 indicate little or no similarity. The MAC values for the wheel are shown in Table 7; modes 1, 2, 3, 4, and 7 have values above 0.97, indicating strong agreement with the FE model. In contrast, modes 5 and 6 have values below 0.93, indicating weaker correlation.

Table 7. Wheel MAC between experimental and FEM mode shapes

	Mode 1	Mode 2	Mode 3	Mode 4	Mode 5	Mode 6	Mode 7
Mode 1	**0.9925**	0.0354	0.0197	0.0172	0.0242	0.0183	0.0191
Mode 2	0.0478	**0.9885**	0.0105	0.0154	0.0024	0.0063	0.0212
Mode 3	0.0203	0.0156	**0.9712**	0.0224	0.019	0.0033	0.0107
Mode 4	0.0199	0.0174	0.009	**0.9736**	0.0159	0.0244	0.0175
Mode 5	0.0081	0.0092	0.0036	0.0138	**0.9171**	0.0133	0.0189
Mode 6	0.0222	0.0091	0.0204	0.0047	0.0124	**0.9311**	0.0166
Mode 7	0.0158	0.0095	0.0066	0.0179	0.0069	0.0221	**0.9874**

The MAC matrix for the rail is presented in Table 8. Modes 1 and 4 correlate well with the FE model, with values exceeding 0.97. However, modes 2 and 3 show lower correlation, with values of 0.8788 and 0.8312, respectively.

Table 8. Rail MAC between experimental and FEM mode shapes

	Mode 1	Mode 2	Mode 3	Mode 4
Mode 1	**0.9808**	0.0407	0.0187	0.0418
Mode 2	0	**0.8788**	0.0444	0
Mode 3	0.0607	0.0651	**0.8312**	0
Mode 4	0.0350	0	0	**0.9979**

3.2 Transient Dynamic Analysis

This section presents and addresses the wheel responses, such as contact pressure, von Mises stress, and nodal lateral displacement.

3.2.1 Nodal contact forces

The nodal contact pressure and von Mises stress in the wheel-contact area were investigated. Figure 13 depicts the contact pressure distribution within the contact patch on the wheel, with four nodes marked in white. Node 3658 exhibits the highest pressure, due to its location at the center of the wheel-rail point of contact; hence, it was chosen for analysis. The peak contact pressure recorded at node 3658, located at the middle of the contact region's ellipse, was 819 MPa. El Alami et al. [45] reported on the influence of rolling and revealed a similar distribution of contact pressure. The contact pressure distribution in our investigation aligns with the findings documented in the literature [46].

The pressure distribution, shown in Figure 13, is elliptical and consistent with Hertzian contact theory. This theory states that when two elastic bodies are in conformal contact, the pressure distribution within the elliptical region can be determined by calculating the semi-axes A and B [47]. To calculate the maximum contact pressure P_m, the positive constants A and B—representing the relative longitudinal and lateral curvature of the wheel and rail—must first be determined using Equations 3 and 4.

$$(A + B) = \frac{1}{2}\left[\frac{1}{R_1^r} + \frac{1}{R_1^t} + \frac{1}{R_2^r} + \frac{1}{R_2^t}\right] = \frac{1}{2}\left[\frac{1}{110\,mm} + \frac{1}{\infty} + \frac{1}{\infty} + \frac{1}{148.79\,mm}\right] = 7.906 \times 10^{-3}\ \text{mm} \tag{3}$$

$$\begin{gathered}(B - A) = \frac{1}{2}\left[\left[\frac{1}{R_1^r} - \frac{1}{R_1^t}\right]^2 + \left[\frac{1}{R_2^r} - \frac{1}{R_2^t}\right]^2 + 2\left[\frac{1}{R_1^r} - \frac{1}{R_1^t}\right]\left[\frac{1}{R_2^r} - \frac{1}{R_2^t}\right] cos2\psi\right]^{1/2} \\ (B - A) = \frac{1}{2}\left[\left[\frac{1}{110\,mm} - \frac{1}{\infty}\right]^2 + \left[\frac{1}{148.79\,mm} - \frac{1}{\infty}\right]^2 + 2\left[\frac{1}{110\,mm} - \frac{1}{\infty}\right]\left[\frac{1}{148.79\,mm} - \frac{1}{\infty}\right] cos2(45)\right]^{1/2} \\ = 5.655 \times 10^{-3}\ \text{mm}\end{gathered} \tag{4}$$

Here, R_1^r and R_2^r denote the rolling radii of the wheel and rail, respectively, while R_1^r and R_2^r represent their lateral radii. The angle ψ denotes the angle between the planes of the wheel and rail rolling radii. The values (A+B) and (B-A) are then computed using Equation 5 to obtain the θ value, which is determined from Hertzian contact stress coefficients m and n. These coefficients, with values 1.9319 and 0.6030 respectively, were obtained by interpolation from the reference table in [48].

$$\begin{aligned}\text{Cos}\,\theta &= \frac{(B - A)}{(A + B)} = \frac{(5.655 \times 10^{-3}\ \text{mm})}{(7.906 \times 10^{-3}\ \text{mm})} = 0.7088 \\ &= \text{Cos}^{-1}\,(0.7088) \\ &= 44.86^\circ\end{aligned} \tag{5}$$

Substituting the values of (A + B), m, and n into the relevant equations yields the lengths of the minor axes a and b, where Fn represents the normal force and E* is the effective modulus of elasticity

$$.a = m\left(\frac{3}{4}\frac{Fn}{E*}\frac{1}{(A + B)}\right)^{1/3} = 1.527\ \text{mm} \tag{6}$$

$$b = n\left(\frac{3}{4}\frac{Fn}{E*}\frac{1}{(A+B)}\right)^{1/3} = 0.477 \text{ mm} \tag{7}$$

The calculated dimensions of a and b are 1.527 mm and 0.477 mm, respectively. The maximum contact pressure P_m at the contact patch was found to be 786 MPa, as calculated using Hertzian contact theory.

$$P_m = \frac{3F}{2\pi ab} = \frac{3(1200)}{2\pi(1.527 \times 0.477)} = 786 \text{ Mpa} \tag{8}$$

A comparison of these results with the FE simulation value of 819 MPa (Table 9) shows an error of only 4%, indicating close agreement between numerical and theoretical results. This confirms that the FE model accurately represents the wheel–rail contact behavior.

Table 9. Wheel MAC between experimental and FEM mode shapes

Descriptions	Hertz Analytical	FEM	Error (%)
Major contact width (a), mm	1.527	1.6186	6 %
Minor contact (b), mm	0.477	0.5152	8 %
Maximum pressure, MPa	786	819	4 %

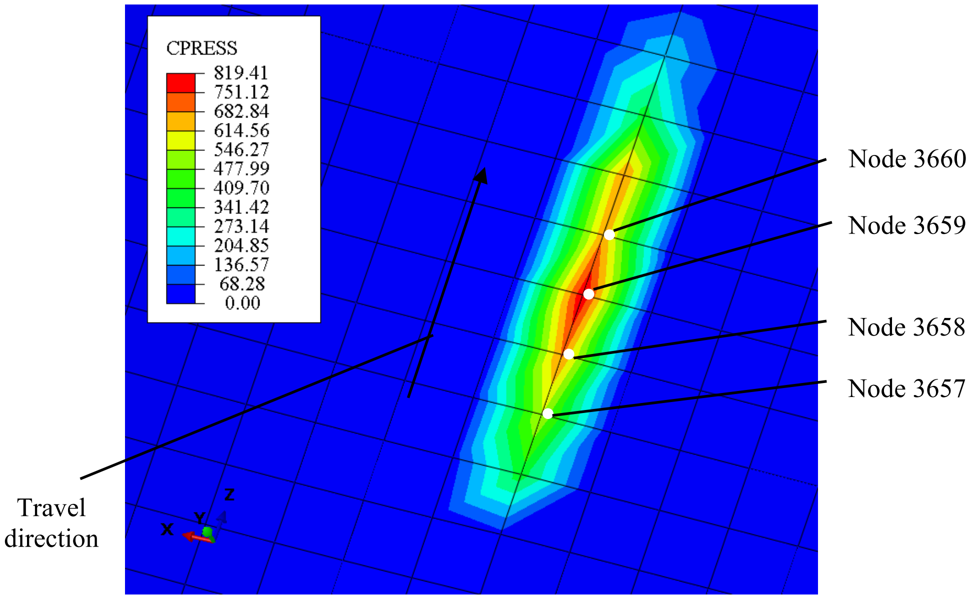

Figure 13. Contact patch observed on the tread of the wheel

The stress at node 3658 peaked at 803 MPa before gradually decreasing as the node exited the contact zone, as illustrated in Figure 14. The contact stress distribution is consistent with prior findings in the literature [49, 50], which indicate that the stress level fluctuates due to the interaction of the wheel and the rail at the contact region.

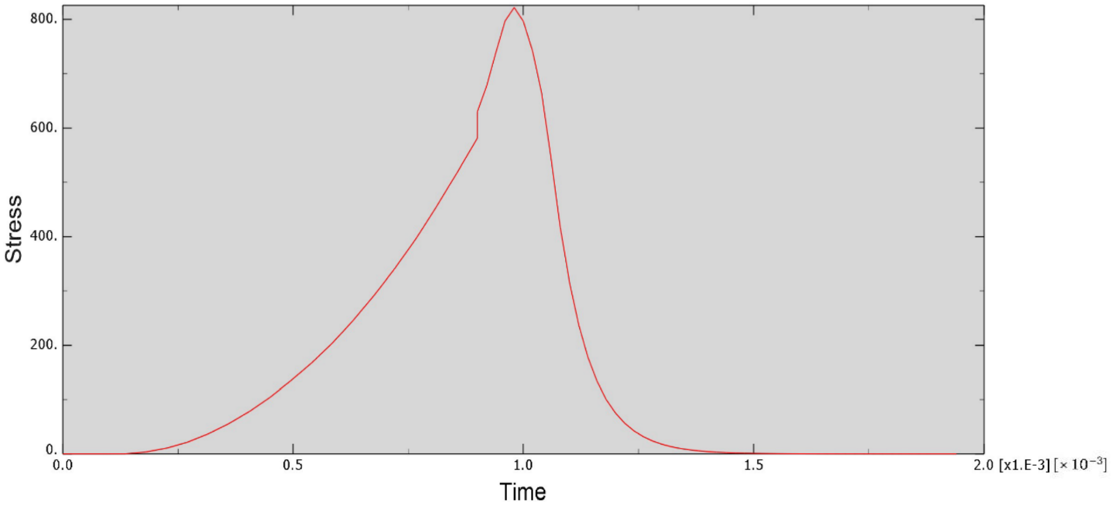

Figure 14. Nodal contact pressure of node 3658

The maximum von Mises stress was 507 MPa, located 1 mm below the tread in the inner contact patch region, and was concentrated on the wheel rather than the rail. As shown in Figure 15, the von Mises stress pattern corresponded to the wheel–rail contact interface contours. The stress increased with higher friction coefficients [51], consistent with tribological studies on tire blocks [52]. The measured stresses were below the yield strength of 545 MPa, indicating no plastic deformation, which could otherwise cause track corrugation. Previous studies [53, 54] have shown that high von Mises stresses in the wheel–rail interface can initiate subsurface cracks and surface alterations, ultimately leading to corrugation.

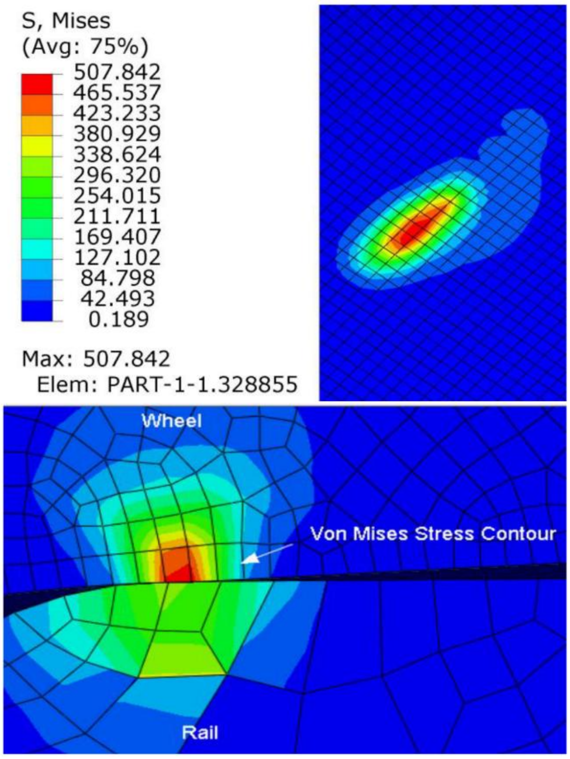

Figure 15. Stress contour of the contact interface

3.2.2 Lateral response

Time-domain analysis is more precise than frequency-domain analysis, as it allows for the incorporation of nonlinearities, such as the lateral creep examined in our study. In this section. The oscillatory response of node 3658 in the lateral direction (X-axis) is assessed for the initiation of stick slip due to lateral creepage with a yaw angle of -3° and a constant friction coefficient of μ = 0.35. A velocity of 0.5 rad/s is applied.

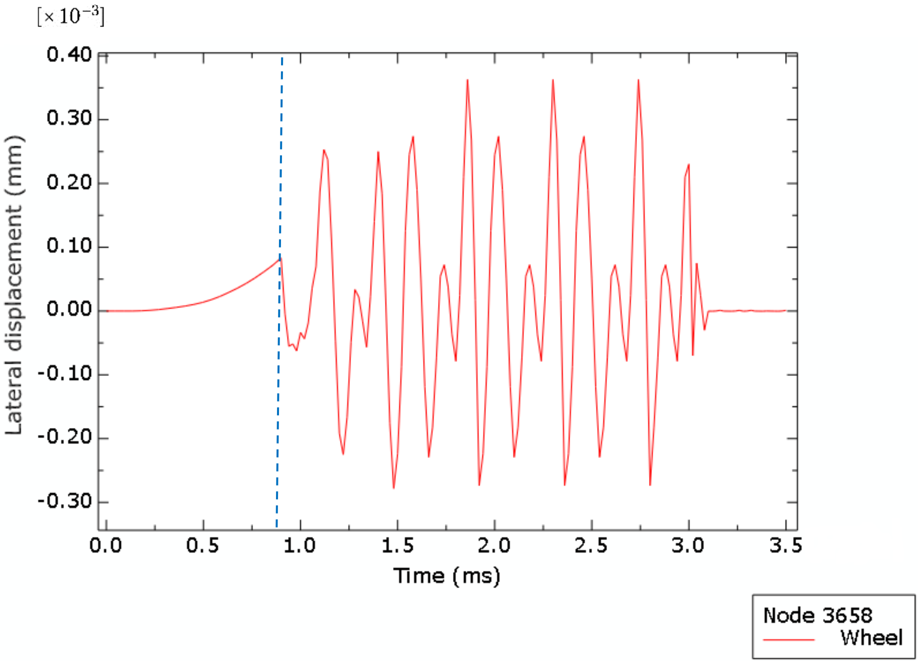

Figure 16. Wheel nodal lateral displacement

Figure 16 illustrates the time-series plot for the wheel generated by Abaqus. The plot illustrates the lateral displacement of node 3658. The plot indicates an oscillating nodal displacement response, exhibiting a maximum peak amplitude of 0.0003 mm when the wheel interacts with the rail. This oscillation response is in accordance with the stick–slip cycle that has been previously characterized in time-domain investigations on railway curve squeal [55,56,57]. The plot indicates the node is in a state of adherence, resisting movement, when the wheel contacts the rail at 0.9 ms (highlighted in blue). As the displacement reached its maximum amplitude, it exceeded the threshold of the static friction coefficient, μ_s, resulting in slippage governed by the dynamic friction coefficient, μ_d, and triggering a periodic transition of stick-slip oscillations. The observed oscillatory response aligns with the notion that the primary cause of stick–slip oscillations is the interplay between vertical and tangential movements contributing to self-excited vibrations that emerge as squeal [30].

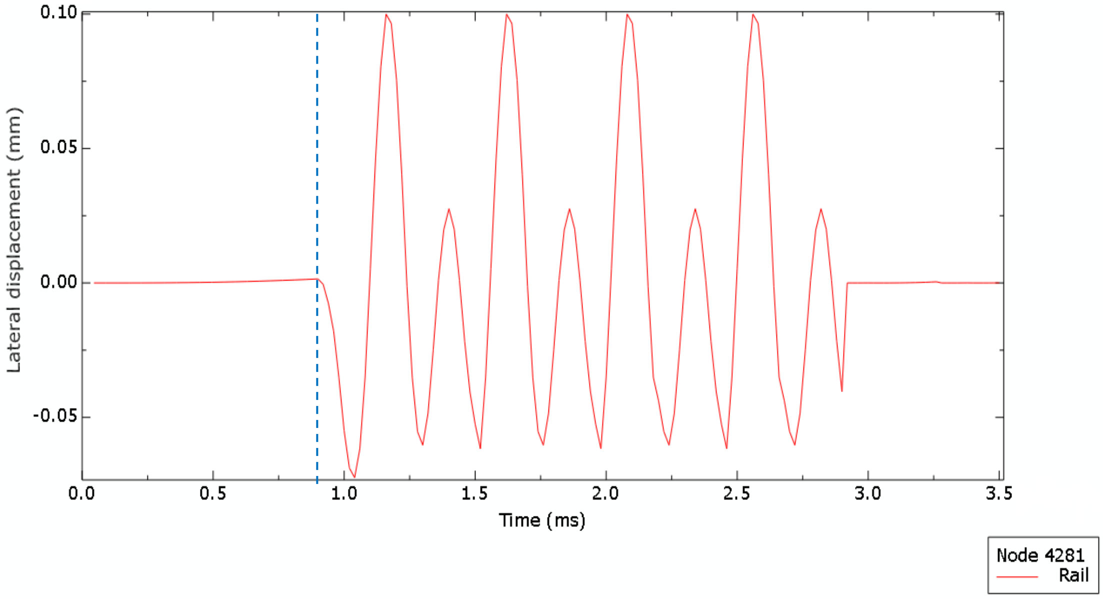

Figure 17. Rail nodal lateral displacement

In addition, the nodal displacement of the rail is examined, as illustrated in Figure 17. A comparable oscillating response was observed in the contact region. Nevertheless, the peak amplitude detected is 0.0001 mm, which is not as pronounced as the peak amplitude of the wheel lateral nodal displacement.

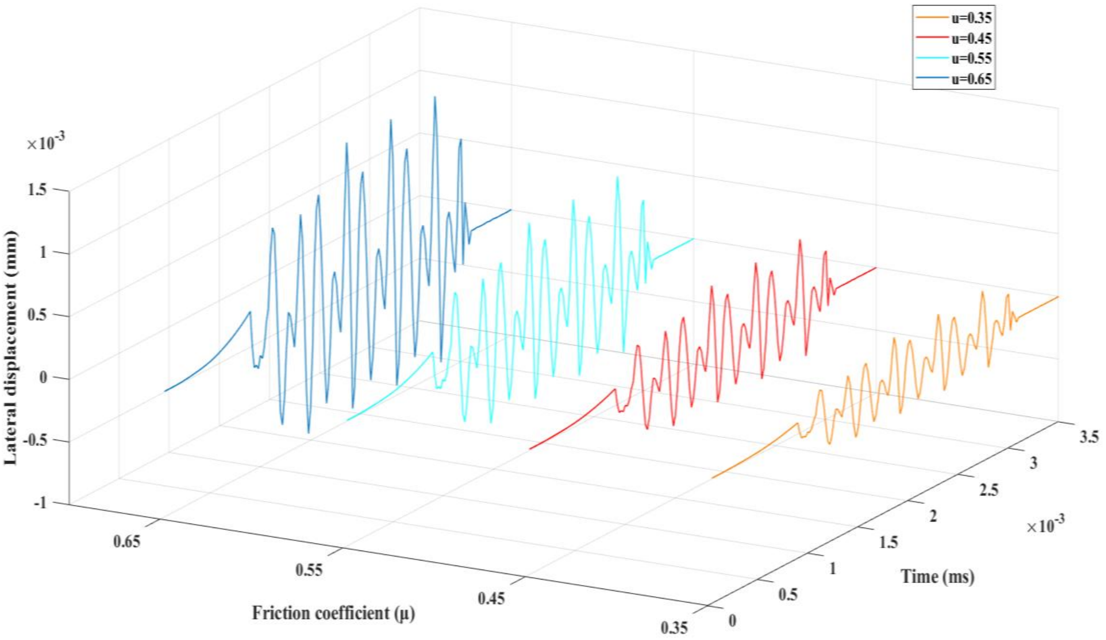

Figure 18. Effects of elevated friction coefficient

To assess the influence of the friction coefficient at the contact interface. A parametric analysis was conducted by varying the friction coefficient. Figure 18 illustrates that the wheel nodal lateral displacement escalated from 0.0003 mm to 0.0013 mm when the friction coefficient increased from μ=0.35 to μ=0.65, indicating a significant increase. This increase demonstrates the evaluation of lateral nodal displacement in the contact region, producing favorable results in identifying system instability associated with elevated friction levels.

3.2.2.1 Validation of the lateral response with squeal measurement

The time history of the nodal lateral displacements from Abaqus is then converted to the frequency domain. We implemented a fast Fourier transform (FFT) technique in MATLAB to analyze the nodal lateral displacements of the system. This facilitated the extraction of corresponding FFT responses, which were obtained and contrasted with the FFT findings from the experiment, acquired from the reduced test rig squeal measurement. The waterfall plot in Figure 19 illustrates the FFT of the nodal lateral displacements for both the rail and wheel. The analysis reveals that the simulated squeal begins at a frequency of 1651 Hz and extends up to 4300 Hz. The FFT analysis of the rail exhibits three peaks at frequencies of 1651,1852, and 4300 Hz. Similarly, the FFT analysis of the wheel reveals four peaks at frequencies of 2350, 2480, 2706, and 2837 Hz. The most prominent peak recorded occurs at 2480 Hz, with a maximum amplitude of 3.5 m/s² for the wheel.

The rail squeal frequency, particularly at 4300 Hz, corresponds to the natural frequencies obtained from experimental modal analysis at 4207 Hz and 4479 Hz. However, Figure 19 indicates that the amplitude at this frequency is significantly lower than that of the wheel squeal frequency. Moreover, the MAC values associated with 4200 Hz and 4479 Hz indicate poor mode shape correlation, suggesting that the rail is not the primary resonator, as the excited natural frequencies do not dominate the overall system response. In contrast, the squeal frequency at 2480 Hz, derived from the FFT of the wheel, shows strong agreement with the natural frequencies of 2393 Hz and 2769 Hz identified in the modal analysis. The wheel mode shapes associated with these frequencies exhibit high similarity, as confirmed by the MAC values in Table 7, indicating that the dominant squeal source is in this range. Thus, the wheel exhibits a higher tendency for self-excitation and serves as a primary resonator during squealing, compared to the rail.

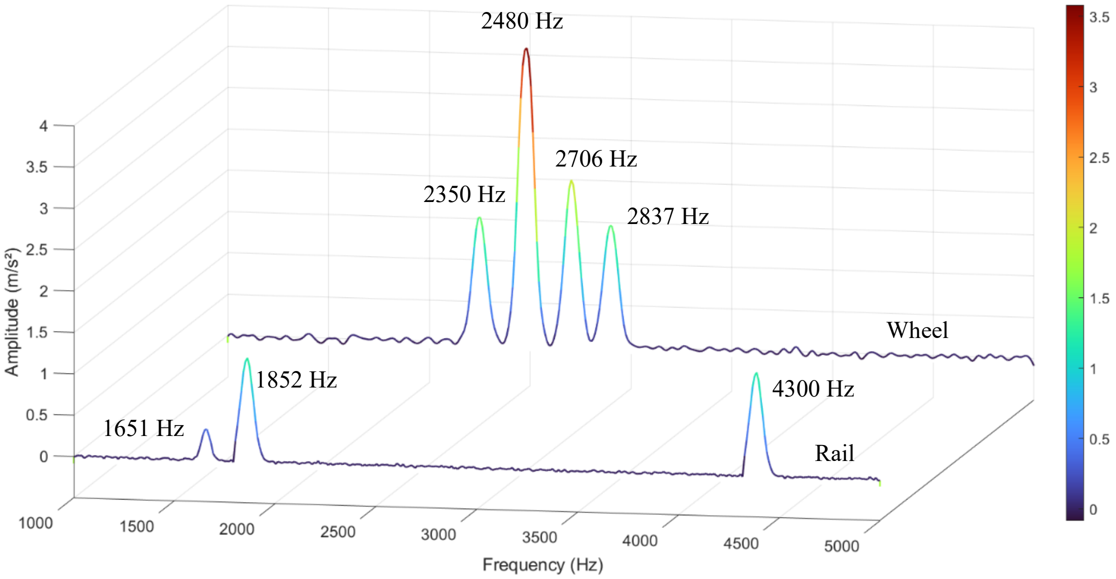

Figure 19. Lateral response FFT

The FFT of the nodal lateral displacement of the wheel was compared and validated against the FFT obtained from the squeal measurement test done under controlled laboratory conditions using the reduced-scale rig, as detailed in the methods section. Figures 20 and 21 depict the FFT of the squeal from the reduced scale rig and the FFT of the wheel obtained from the transient analysis. The FFT plots indicate that the most dominant squeal frequencies identified were at 2400 Hz and 2480 Hz, which match the wheel's natural frequency at 2769 Hz. Consequently, it can be asserted that displacements in the lateral direction excited the wheel mode at the natural frequency of 2769 Hz, resulting in a resonant mode. The amplitude difference between the transient analysis and experiment was approximately 3.33%. The squeal measurement validated the transient analysis results of the nodal lateral displacement, specifically node 3658.

The transient analysis revealed encouraging outcomes by identifying system instability caused by lateral creepage resulting from an enforced yaw angle, which mimics a curved behavior. The findings indicated that the stick-slip oscillation observed in the lateral nodal displacement of the wheel at a yaw angle of −3° is the cause of the excitation frequency that manifests as squeal.

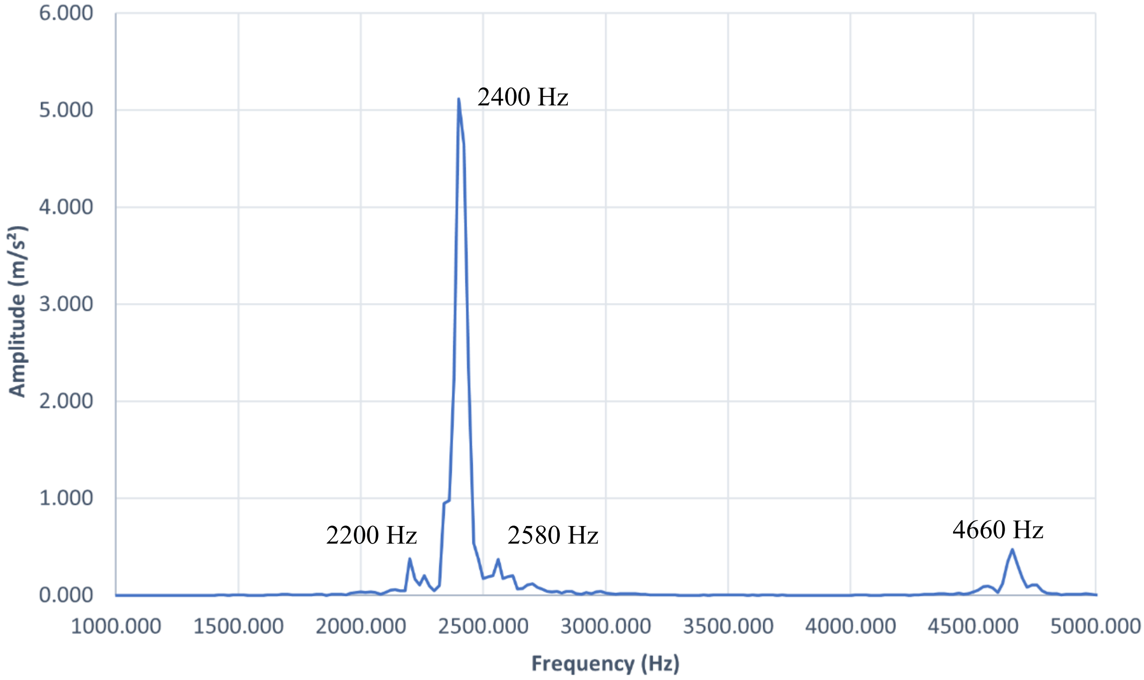

Figure 20. Squeal measurement FFT

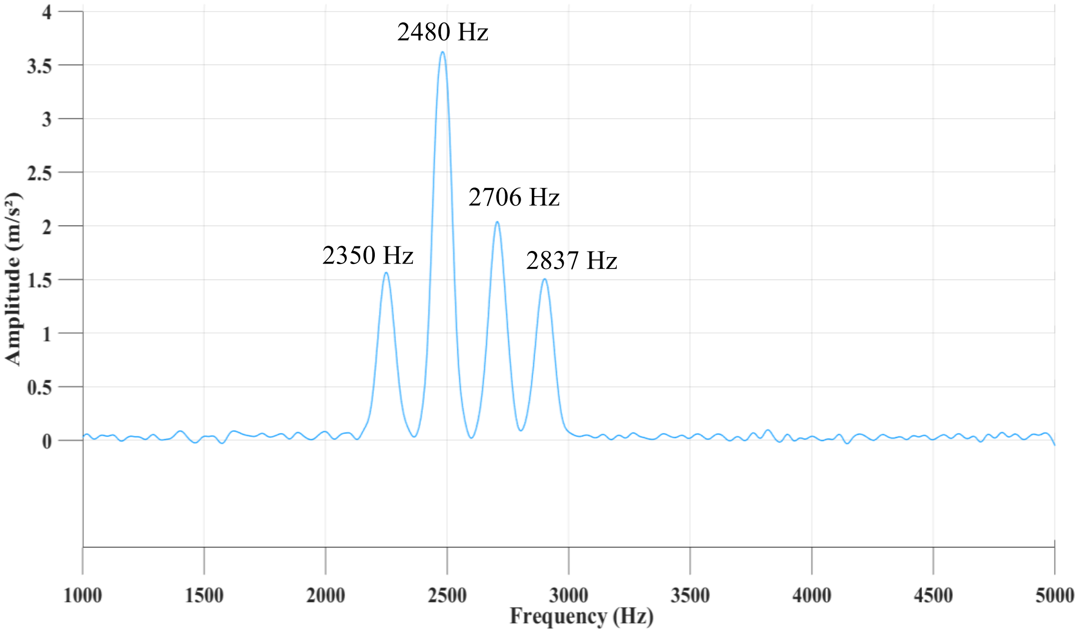

Figure 21. Wheel lateral response FFT

4. CONCLUSION

In this study, the wheel–rail interaction was investigated using an FE approach to simulate rolling conditions with a predetermined yaw angle, replicating the behavior observed during curving. The FE model results showed strong agreement with experimental findings. Nonlinear time-domain transient analysis yielded favorable results for nodal lateral displacement of the wheel-rail system, confirming the presence of lateral sliding (stick–slip phenomenon) under constant friction between the wheel and rail interaction. The lateral displacement of the nodes was found to excite the natural mode of the wheel, producing a resonant response that amplified the squeal. Assuming a constant friction coefficient, the findings indicate that curve squeal occurs from the continuous stick–slip phenomenon, which constantly induces the wheel–rail system. The resulting high-amplitude vibration responsible for squeal is attributed to an oscillatory limit cycle.

ACKNOWLEDGEMENTS

This research was funded under the Fundamental Research Grant Scheme (FRGS) (304.PMEKANIK.6050379) by the Ministry of Science, Technology and Innovation (MOSTI). We convey our appreciation to the University of Sains Malaysia (USM) for its substantial assistance. Also, we would like to express appreciation to Mr. Baharom Awang and Mr. Wan Muhammad Amri for their support in the Vibration Lab.

CONFLICT OF INTEREST

The authors declare that they have no conflicts of interest.

AUTHOR CONTRIBUTIONS

Zaidi Mohd Ripin: Conceptualization, methodology, investigation, writing – review & editing, supervision

Charvinder Singh: Methodology, software, investigation, formal analysis, data curation, writing – original draft

Nurul Farhana Mohd Yusuf: Formal analysis, investigation, writing – review & editing, supervision

Muhammad Fauzinizam Razali: Investigation, software, formal analysis, writing – review & editing

Muhammad Najib Abdul Hamid: methodology, software, investigation, writing – review & editing

REFERENCES

[1] A. D. Monk-Steel, D. J. Thompson, F. G. De Beer, and M. H. A. Janssens, “An investigation into the influence of longitudinal creepage on railway squeal noise due to lateral creepage,” *Journal of Sound and Vibration*, vol. 293, no. 3–5, pp. 766–776, 2006.

[2] M. N. A. Hamid, C.-Y. Teoh, and Z. M. Ripin, “The operational deflection shapes and transient analysis of the brake shoes in drum brake squeal,” *Proceedings of the Institution of Mechanical Engineers Part D Journal of Automobile Engineering*, vol. 227, no. 6, pp. 866–884, 2013.

[3] Y. Gao, G. Zhang, M. Yuan, J. Ji, N. Cui, and S. Huang, “The numerical study for the effect of stiffness matching on Wheel–Rail Curve Squeal noise,” *Applied Sciences*, vol. 13, no. 21, p. 11615, 2023.

[4] P. T. Torstensson, A. Pieringer, M. Höjer, R. Nilsson, and V. Simonsson, “A case study of railway curve squeal radiated from both the outer and inner wheel,” *Applied Acoustics*, vol. 228, p. 110327, 2024.

[5] S. R. Marjani and D. Younesian, “Active vibration control for the mitigation of wheel squeal noise based on a fuzzy Self-Tuning PID controller,” *Shock and Vibration*, vol. 2022, pp. 1–17, 2022.

[6] G. Zhou, C. He, G. Wen, and Q. Liu, “Fatigue damage mechanism of railway wheels under lateral forces,” *Tribology International*, vol. 91, pp. 160–169, 2015.

[7] V. T. Andrés, J. Martínez-Casas, F. D. Denia, D. J. Thompson, and S. Bruni, “Railway rolling noise in curved tracks: Dynamic modelling of the wheelset and influence of the curve,” *Journal of Sound and Vibration*, p. 118738, 2024.

[8] F. Castellini *et al.*, “Curve squeal in sharp curves: effect of multiple wheel/rail contact points,” *Applied Acoustics*, vol. 218, p. 109862, 2024.

[9] P. Zhang, G. Krishnan, and Z. Yang, “An experimental and numerical study on the generation of wheel-rail stick–slip contact behaviour,” *Intelligent Transportation Infrastructure*, 2025.

[10] X. Feng, G. Chen, B. Dong, Q. Song, and W. Ren, “Study on the generation mechanism of curve squeal and its relationship with wheel/rail wear,” *Proceedings of the Institution of Mechanical Engineers Part F Journal of Rail and Rapid Transit*, vol. 238, no. 9, pp. 1084–1095, 2024.

[11] M. J. Rudd, “Wheel/rail noise—Part II: Wheel squeal,” *Journal of Sound and Vibration*, vol. 46, no. 3, pp. 381–394, 1976.

[12] A. Wickens, Fundamentals of Rail Vehicle Dynamics, CRC Press, 2003.

[13] J. J. Kalker, “Wheel-rail rolling contact theory,” *Wear*, vol. 144, no. 1–2, pp. 243–261, 1991.

[14] B. Ding, G. Squicciarini, D. Thompson, and R. Corradi, “An assessment of mode-coupling and falling-friction mechanisms in railway curve squeal through a simplified approach,” *Journal of Sound and Vibration*, vol. 423, pp. 126–140, 2018.

[15] X. Liu and P. A. Meehan, “Wheel squeal noise: A simplified model to simulate the effect of rolling speed and angle of attack,” *Journal of Sound and Vibration*, vol. 338, pp. 184–198, 2014.

[16] D. J. Thompson, G. Squicciarini, B. Ding, and L. Baeza, “A State-of-the-Art Review of Curve squeal Noise: Phenomena, Mechanisms, Modelling and Mitigation,” *Notes on Numerical Fluid Mechanics and Multidisciplinary Design*, pp. 3–41, 2018.

[17] A. Alonso, A. Guiral, L. Baeza, and S. Iwnicki, “Wheel–rail contact: experimental study of the creep forces–creepage relationships,” Vehicle System Dynamics, vol. 52, no. sup1, pp. 469–487, 2014.

[18] Z. Huang, “Theoretical modelling of railway curve Squeal,” Doctoral dissertation, University of Southampton, 2007.

[19] G. Xie, P. D. Allen, S. D. Iwnicki, A. Alonso, D. J. Thompson, C. J. C. Jones, et al., “Introduction of falling friction coefficients into curving calculations for studying curve squeal noise,” *Vehicle System Dynamics*, vol. 44, no. sup1, pp. 261–271, 2006.

[20] F. G. De Beer, M. H. A. Janssens, and P. P. Kooijman, “Squeal noise of rail-bound vehicles influenced by lateral contact position,” *Journal of Sound and Vibration*, vol. 267, no. 3, pp. 497–507, 2003.

[21] X. Liu and P. A. Meehan, "Investigation of the effect of lateral adhesion and rolling speed on wheel squeal noise," *Proceedings of the Institution of Mechanical Engineers Part F Journal of Rail and Rapid Transit*, vol. 227, no. 5, pp. 469–480, 2013.

[22] A. Anyakwo, "Condition monitoring of curve squeal based on analysis of acoustic and vibration data," Doctoral dissertation, University of Huddersfield, 2020.

[23] V. Navrátil, R. Galas, M. Klapka, D. Kvarda, and M. Omasta, "Wheel squeal mitigation under water lubrication," *Tribology in Industry*, vol. 46, no. 3, p. 418, 2024.

[24] V. Navrátil, R. Galas, M. Klapka, D. Kvarda, M. Omasta, L. Shi, et al., "Wheel squeal noise in rail transport: The effect of friction modifier composition," *Tribology in Industry*, vol. 44, no. 3, pp. 361–373, 2022.

[25] X. Liu and P. A. Meehan, "Investigation of squeal noise under positive friction characteristics condition provided by friction modifiers," *Journal of Sound and Vibration*, vol. 371, pp. 393–405, 2016.

[26] D. J. Thompson, G. Squicciarini, B. Ding, and L. Baeza, "A State-of-the-Art Review of Curve squeal Noise: Phenomena, Mechanisms, Modelling and Mitigation," *Notes on Numerical Fluid Mechanics and Multidisciplinary Design*, pp. 3–41, 2018.

[27] J. C. Kim, H.-M. Noh, and Y. S. Yun, "Local coating of curved rails by using low friction material for squeal noise reduction," *Advances in Mechanical Engineering*, vol. 12, no. 12, p. 168781402098065, 2020.

[28] Y. Zhang, X. Xiao, H. Shen, Y. Li, B. Wang, and X. Jin, "The effect of ring dampers on noise radiation from railway wheels," *Noise Control Engineering Journal*, vol. 60, no. 3, pp. 293–300, 2012.

[29] I. Zenzerovic and Ivan Zenzerovic, "Engineering model for curve squeal formulated in the time domain," Chalmers Tekniska Hogskola: Sweden, 2014.

[30] A. Pieringer, "A numerical investigation of curve squeal in the case of constant wheel/rail friction," *Journal of Sound and Vibration*, vol. 333, no. 18, pp. 4295–4313, 2014.

[31] A. Pieringer, P. Torstensson, J. Theyssen, and W. Kropp, "Transient modelling of curve squeal considering varying contact conditions," in *Lecture Notes in Mechanical Engineering*, pp. 491–499, 2024.

[32] W. Kropp, J. Theyssen, and A. Pieringer, "The application of dither to mitigate curve squeal," *Journal of Sound and Vibration*, vol. 514, p. 116433, 2021.

[33] E. Schneider, K. Popp, and H. Irretier, "Noise generation in railway wheels due to rail-wheel contact forces," *Journal of Sound and Vibration*, vol. 120, no. 2, pp. 227–244, 1988.

[34] M. A. Heckl and I. D. Abrahams, "Curve squeal of train wheels, part 1: mathematical model for its generation," *Journal of Sound and Vibration*, vol. 229, no. 3, pp. 669–693, 2000.

[35] M. A. Heckl, "Curve squeal of train wheels: unstable modes and limit cycles," Proceedings of the Royal Society a Mathematical Physical and Engineering Sciences, vol. 458, no. 2024, pp. 1949–1965, 2002.

[36] Ch. Glocker, E. Cataldi-Spinola, and R. I. Leine, "Curve squealing of trains: Measurement, modelling and simulation," *Journal of Sound and Vibration*, vol. 324, no. 1–2, pp. 365–386, 2009.

[37] A. Pieringer, P. Torstensson, and J. Giner, "Curve squeal of rail vehicles: Linear stability analysis and nonlinear time-domain simulation," in *Proceedings of the Third International Conference on Railway Technology: Research, Development and Maintenance*, Civil-Comp Press, Stirlingshire, Scotland, 2016.

[38] D. J. Thompson, G. Squicciarini, B. Ding, L. Baeza, "A state-of-the-art review of curve squeal noise: phenomena, mechanisms, modelling and mitigation," in: D. Anderson et al. (Eds.), Noise and Vibration Mitigation for Rail Transportation Systems, Notes on Numerical Fluid Mechanics and Multidisciplinary Design, Springer, 2018, pp. 1-9.

[39] D. T. Eadie, M. Santoro, and J. Kalousek, "Railway noise and the effect of top of rail liquid friction modifier," *Proceedings of the 6th International Conference on Contact Mechanics and Wear of Rail/Wheel Systems (CM2003)*, Vol. II, Gothenburg, Sweden, June 10-13, 2003, pp. 503-510.

[40] T. Hidayat, R. Ismail, M. Tauviqirrahman, E. Saputra, M. I. Ammarullah, M. D. Lamura, et al., "Investigation of mesh model for a finite element simulation of the dual-mobility prosthetic hip joint," *Jurnal Tribologi*, vol. 38, pp. 118–140, 2023.

[41] "Siemens Digital Industries Software Community." https://community.sw.siemens.com/s/article/Modal-Stabilization-Diagram-Tips

[42] J. Lau, J. Lanslots, B. Peeters, and H. Van der Auweraer, "Automatic modal analysis: Reality or myth?" *VDI Berichte 1982*, p. 103, 2007.

[43] S. Chauhan and D. Tcherniak, "Clustering approaches to automatic modal parameter estimation," in *Proceedings, International Modal Analysis Conference* (IMAC), 2008.

[44] V. Srivastava, K. Patil, J. Baqersad, and J. Zhang, "A multi-view DIC approach to extract operating mode shapes of structures," in *Conference proceedings of the Society for Experimental Mechanics*, pp. 43–48, 2018.

[45] M. R. Aalami, A. Anari, T. Shafighfard, and S. Talatahari, "A robust finite element analysis of the Rail-Wheel rolling contact," *Advances in Mechanical Engineering*, vol. 5, p. 272350, 2013.

[46] R. A. Ibrahim, "Friction-induced vibration, chatter, squeal, and chaos—Part II: Dynamics and Modeling," *Applied Mechanics Reviews*, vol. 47, no. 7, pp. 227–253, 1994.

[47] V. Kosarchuk, V. Tverdomed, and O. Bambura, "Calculation schemes for determining contact stresses in railway rails," *Applied Sciences*, vol. 15, no. 6, p. 2970, 2025.

[48] P. Urassa, H. S. Habte, and A. Mohammedseid, "Crack influence and fatigue life assessment in rail profiles: A numerical study," *Frontiers in Built Environment*, vol. 9, p. 1304557, 2023.

[49] P. T. Zwierczyk and K. Váradi, “Frictional contact FE analysis in a railway wheel-rail contact,” *Periodica Polytechnica Mechanical Engineering*, vol. 58, no. 2, pp. 93–99, 2014.

[50] R. S. Ashofteh and A. Mohammadnia, “Stress analysis in the Elastic-Plastic analysis of railway wheels,” *International Journal of Railway*, vol. 7, no. 1, pp. 1–7, 2014.

[51] B. C. Goo and J. C. Kim, “Complex eigenvalue analysis of railway wheel/rail squeal,” *International Journal of Engineering Science and Technology*, vol. 8, no. 1, pp. 1–12, 2016.

[52] B. Setiyana, M. Muchammad, M. Tauviqirrahman, J. Jamari, and Eko Saputra, “The tribological performance identification of a tire tread block during friction contact: A numerical investigation,” vol. 41, pp. 81-92, 2024.

[53] S. Zhang, Z. Sun, and F. Guo, “Investigation on wear and contact fatigue of involute modified gears under minimum quantity lubrication,” *Wear*, vol. 484–485, p. 204043, 2021.

[54] G. G. Sirata, H. G. Lemu, K. Waclawiak, and Y. D. Jelila, “Study of rail-wheel contact problem by analytical and numerical approaches,” *IOP Conference Series Materials Science and Engineering*, vol. 1201, no. 1, p. 012035, 2021.

[55] J. Giner-Navarro, J. Martínez-Casas, F. D. Denia, and L. Baeza, “Study of railway curve squeal in the time domain using a high-frequency vehicle/track interaction model,” *Journal of Sound and Vibration*, vol. 431, pp. 177–191, 2018.

[56] A. Pieringer, L. Baeza, and W. Kropp, “Modelling of railway curve squeal including effects of wheel rotation,” in *Notes on Numerical Fluid Mechanics and Multidisciplinary Design*, pp. 417–424, 2014.

[57] G. Popa, M. Andrei, E. Tudor, I. Vasile, and G. Ilie, “Fast detection of the stick–slip phenomenon associated with wheel-to-rail sliding using acceleration sensors: An experimental study,” *Technologies*, vol. 12, no. 8, p. 134, 2024.